1 **Weakened aerosol-radiation interaction exacerbating ozone**

2 **pollution in eastern China since China's clean air actions**

3

4 Hao Yang[1,2], Lei Chen[1], Hong Liao[1], Jia Zhu[1], Wenjie Wang[3], Xin Li[3]

5

6 [1]Jiangsu Key Laboratory of Atmospheric Environment Monitoring and Pollution

7 Control, Jiangsu Collaborative Innovation Center of Atmospheric Environment and

8 Equipment Technology, School of Environmental Science and Engineering, Nanjing

9 University of Information Science & Technology, Nanjing 210044, China

10 [2]College of Materials Science and Engineering, Guizhou Minzu University, Guiyang

11 550025, China

12 [3]State Joint Key Laboratory of Environmental Simulation and Pollution Control,

13 College of Environmental Sciences and Engineering, Peking University, Beijing

14 100871, China

15

16 **Correspondence to:** Lei Chen (chenlei@nuist.edu.cn) and Hong Liao

17 (hongliao@nuist.edu.cn)

18

19

20 **Abstract**

21   Since China's clean air action, $PM_{2.5}$ air quality has been improved while ozone

22 (O_3) pollution has been becoming severe. Here we apply a coupled meteorology-

23 chemistry model (WRF-Chem) to quantify the responses of aerosol-radiation

24 interaction (ARI), including aerosol-photolysis interaction (API) and aerosol-radiation

25 feedback (ARF), to anthropogenic emission reductions from 2013 to 2017, and their

26 contributions to O_3 increases over eastern China in summer and winter. Sensitivity

27 experiments show that the decreased anthropogenic emissions play a more prominent

28 role for the increased MDA8 O_3 both in summer (+1.96 ppb vs. +0.07 ppb) and winter

29 (+3.56 ppb vs. -1.08 ppb) than the impacts of changed meteorological conditions. The

30 decreased $PM_{2.5}$ caused by emission reduction can result in a weaker impact of ARI on

31 O_3 concentrations, which poses a superimposed effect on the worsened O_3 air quality.

32 The weakened ARI due to decreased anthropogenic emission aggravates the summer

33 (winter) O_3 pollution by +0.81 ppb (+0.63 ppb) averaged over eastern China, with

34 weakened API and ARF contributing 55.6% (61.9%) and 44.4% (38.1%), respectively;

35 this superimposed effect is more significant for urban areas during summer (+1.77 ppb).

36 Process analysis indicates that the enhanced chemical production is the dominant

37 process for the increased O_3 concentrations caused by weakened ARI both in summer

38 and winter. This study innovatively reveals the adverse effect of weakened aerosol-

39 radiation interaction due to decreased anthropogenic emissions on O_3 air quality; more

40 stringent coordinated air pollution control strategies are needed for future air quality

41 improvement.

42

1. Introduction

With the implementation of clean air action since 2013, $PM_{2.5}$ (particulate matter with an aerodynamic equivalent diameter of 2.5 micrometers or less) concentrations have decreased significantly in China (Zhai et al., 2019; Zhang et al., 2019). However, ozone (O_3) pollution is becoming worse and poses a significant challenge over eastern China, especially in the developed city clusters including Beijing-Tianjin-Hebei (BTH), Yangtze River Delta (YRD), Pearl River Delta (PRD), and Sichuan Basin (SCB) (Lu et al., 2018; Dang and Liao, 2019; Li et al., 2019; Li et al., 2021). According to observation data, Li et al. (2020) found that the daily maximum 8-h average O_3 concentrations (MDA8 O_3) increased at a rate of 1.9 ppb a^{-1} from 2013 to 2019 over eastern China. Elevated O_3 concentrations can not only decrease crop yield but also damage human health (Lelieveld et al., 2015; Yue et al., 2017; Mills et al., 2018). Therefore, it is essential to gain a comprehensive understanding about factors driving the increasing trend of O_3 in China in order to formulate effective prevention strategies.

As a secondary air pollutant, troposphere O_3 can be produced by nitrogen oxides (NO_x = NO + NO_2) and volatile organic compounds (VOCs) in the presence of solar radiation through photochemical reactions (Atkinson, 2000; Seinfeld and Pandis, 2006). Consequently, the concentration of O_3 is closely related to changes in meteorological conditions and anthropogenic emissions (Wang et al., 2019; Liu and Wang, 2020a,b; Shu et al., 2020). Moreover, particulates can also affect O_3 concentrations through aerosol-radiation interaction (ARI), including aerosol-photolysis interaction (API) and aerosol-radiation feedback (ARF) (Liao et al., 1999; Wang et al., 2016; Zhu et al., 2021; Yang et al., 2022), and heterogeneous chemistry on aerosol surface (Lou et al., 2014; Li et al., 2019; Liu and Wang, 2020b). Many studies have found that the decreased $PM_{2.5}$ can be one of the driving factors contributing to the increased O_3 concentrations (Li et al., 2019; Liu and Wang, 2020b; Shao et al., 2021). Li et al. (2019) analyzed GEOS-Chem simulation results and pointed out that the reductions in $PM_{2.5}$ concentrations from 2013 to 2017 in North China Plain (NCP) could decrease the sink of HO_2 on aerosol surface, which would result in the increase in O_3 concentrations.

72   When heterogeneous reactions were considered in WRF-CMAQ, Liu and Wang (2020b)

73   found that decreased $PM_{2.5}$ concentrations weakened the uptake of reactive gases

74   (mainly HO_2 and O_3) which led to the increase in O_3 concentrations over China from

75   2013 to 2017. However, the contribution of weakened aerosol-radiation interaction due

76   to substantial decreases in $PM_{2.5}$ under clean air action to the increased O_3 has not been

77   systematically quantified. Furthermore, previous studies mainly focus on the increased

78   summer O_3 (Li et al., 2019; Liu and Wang, 2020a,b; Shu et al., 2020; Shao et al., 2021),

79   but underlying reasons driven the changes in winter O_3 is unclear. Li et al. (2021)

80   pointed out that O_3 pollution has been extended into cold seasons under the emission

81   control measures. Therefore, this study aims to quantify the response of aerosol-

82   radiation interaction to anthropogenic emission reduction from 2013 to 2017, with the

83   mainly focus on the contribution to changed O_3 concentrations over eastern China both

84   in summer and winter.

85   Aerosol-radiation interaction (ARI) can alter photolysis rates through aerosol-

86   photolysis interaction (API) and meteorological variables through aerosol-radiation

87   feedback (ARF) to suppress O_3 formation (Yang et al., 2022). Hong et al. (2020) used

88   WRF-CMAQ in conjunction with future emission scenarios to find that weakened ARF

89   due to reduced aerosol concentration led to an increase in the daily maximum 1-h

90   average O_3 concentration in eastern China from 2010 to 2050. By using WRF-CMAQ,

91   Liu and Wang (2020b) reported that weakened API could increase the MDA8 O_3

92   concentrations by 0.3 ppb in urban areas from 2013 to 2017. Zhu et al. (2021) used

93   WRF-Chem to investigate the impact of weakened ARF on air pollutants over NCP

94   during COVID-19 lockdown and reported that the weakened ARF would increase the

95   O_3 concentrations by 7.8%. In general, previous studies mainly examined the impact of

96   either weakened ARF or API, systematic analysis about the total and the respective

97   impacts of changed API and/or ARF on O_3 over eastern China both in summer and

98   winter from 2013 to 2017 have not been conducted.

99   The objective of this manuscript is to examine the impacts of aerosol-radiation

100   interactions (ARI), including the effects of aerosol-photolysis interaction (API) and

101   aerosol-radiation feedback (ARF), on O_3 concentrations over eastern China both in

102 summer and winter by using the online coupled WRF-Chem model, with the main focus

103 on their responses to clean air action. Process analysis is also applied to explore the

104 prominent physical/chemical process responsible for the changed impacts of API and/or

105 ARF on surface O_3. This study is believed to provide insights into the role of weakened

106 ARI on O_3 levels over eastern China not only in summer, but also in winter. In Section

107 2, we describe the model configuration, numerical experiments, observational data, and

108 the integrated process rate analysis. Model evaluation is presented in Section 3. The

109 presentation of model results and the corresponding analyses are exhibited in Section

110 4. Conclusions are provided in Section 5.

111 **2. Methodology**

112 2.1 Model configuration

113   The model used in this study is an online-coupled meteorology-chemistry model,

114 Weather Research and Forecasting with Chemistry model (WRF-Chem v3.7.1), that

115 can simulate meteorological fields and concentrations of gases and aerosols

116 simultaneously (Grell et al., 2005; Skamarock et al., 2008). Figure S1 shows the

117 simulated domain that covers most regions of China with a horizontal resolution of 27

118 km and grid points of 167 (west–east) × 167 (south–north). The model contains 32

119 vertical levels extending from the surface to 50 hPa, with the first 16 layers located

120 below 2 km to resolve fine boundary layer processes. The enclosed black line in Figure

121 S1 represents the eastern China (22-41.5 °N, 102-123 °E), and the four heavily polluted

122 regions are also selected for analysis, including BTH (36.0-41.5 °N, 113-119.5 °E),

123 YRD (29.5-32.5 °N, 118-122 °E), PRD (21-23.5 °N, 112-116 °E), and SCB (27.5-

124 31.5 °N, 102.5-107.5 °E), respectively.

125   The National Center for Environmental Prediction (NCEP) Final Analysis dataset

126 (FNL) with a spatial resolution of 1° × 1° and 6-hour temporal resolution are used to

127 provide the meteorological initial and lateral boundary conditions. The chemical initial

128 and boundary conditions for the WRF-Chem model are taken from the outputs of

129 Community Atmosphere Model with Chemistry (CAM-Chem).

130   The Carbon Bond Mechanism Z (CBM-Z) is applied as the gas-phase chemical

131   mechanism (Zaveri and Peters, 1999), and the full 8-bin MOSAIC (Model for

132   Simulating Aerosol Interactions and Chemistry) aerosol module with aqueous

133   chemistry is used to simulate aerosol evolution (Zaveri et al., 2008). In MOSAIC

134   module, aerosols are assumed to be internally mixed into 8 bins (0.039–0.078 μm,

135   0.078–0.156 μm, 0.156–0.312 μm, 0.312–0.625 μm, 0.625–1.25 μm, 1.25–2.5 μm, 2.5–

136   5.0 μm and 5.0–10 μm), and each bin considers all major aerosol species, such as sulfate

137   (SO_4^{2-}), nitrate (NO_3^-), ammonium (NH_4^+), black carbon (BC), organic carbon (OC), and

138   other inorganic mass (secondary organic aerosols are not included in MOSAIC (Yang

139   et al., 2022)). The impacts of aerosols on photolysis rates are calculated by using the

140   Fast-J scheme (Wild et al., 2000). The following physical parameterizations are used in

141   WRF-Chem. The Rapid Radiative Transfer Model for general circulation models

142   (RRTMG) scheme is used to treat both shortwave and longwave radiation in the

143   atmosphere (Iacono et al., 2008). The Purdue Lin microphysics scheme (Lin et al., 1983)

144   and the Grell 3D ensemble scheme (Grell, 1993) are used to describe the cloud

145   microphysical and cumulus convective processes. The Noah land surface scheme (Chen

146   and Dudhia, 2001) and the Monin-Obukhov surface scheme (Foken, 2006) are used to

147   simulate land-atmosphere interactions. The planetary boundary layer is characterized

148   by Yonsei University PBL scheme (Hong et al 2006).

149   In this study, Multi-resolution Emission Inventory for China (MEIC;

150   http://www.meicmodel.org/) in 2013 and 2017 are used as the anthropogenic emissions

151   of particles and gases (Zheng et al., 2018). Biogenic emissions are calculated online by

152   using the Model of Emissions of Gases and Aerosols from Nature (MEGAN) developed

153   by Guenther et al. (2006).

154   2.2 Numerical experiments

155   Seven sensitivity experiments are designed (Table 1). Here are the detailed

156   descriptions:

157   (1) BASE_17E17M: This baseline experiment is coupled with the interactions

158   between aerosol and radiation, which includes the impacts of API and ARF. Both

159   the meteorological field and anthropogenic emission are fixed at year 2017.

160 (2) BASE_13E13M: Same as BASE_17E17M, but the meteorological field and

161 anthropogenic emission are fixed at year 2013.

162 (3) NOAPI_17E17M: Same as BASE_17E17M, but the impact of API is not

163 considered by turning off the aerosol effect in the photolysis module, following the

164 method described in Yang et al. (2022).

165 (4) NOALL_17E17M: Same as BASE_17E17M, but neither the impact of API nor

166 ARF is considered by zeroing the aerosol optical properties in the optical module,

167 following the method described in Yang et al. (2022).

168 (5) BASE_13E17M: Same as BASE_17E17M, but the anthropogenic emission is

169 fixed at year 2013.

170 (6) NOAPI_13E17M: Same as NOAPI_17E17M, but the anthropogenic emission is

171 fixed at year 2013.

172 (7) NOALL_13E17M: Same as NOALL_17E17M, but the anthropogenic emission is

173 fixed at year 2013.

174 Figure 1 detailedly presents the schematic overview of designed numerical

175 experiments. As shown in Fig. 1, the differences between BASE_17E17M and

176 BASE_13E13M (BASE_17E17M minus BASE_13E13M) represent the changed O_3

177 (ΔO_3) due to variations in meteorology and anthropogenic emissions from 2013 to 2017.

178 The differences between BASE_13E17M and BASE_13E13M (BASE_13E17M minus

179 BASE_13E13M) show the impact of changed meteorological conditions on O_3

180 (ΔO_3_MET) from 2013 to 2017. The differences between BASE_17E17M and

181 BASE_13E17M (BASE_17E17M minus BASE_13E17M) indicate the impact of

182 anthropogenic emission reductions on O_3 (ΔO_3_EMI) from 2013 to 2017.

183 The impacts of aerosol-radiation interaction (ARI) on O_3 under different

184 anthropogenic emission scenarios (i.e., strong anthropogenic emission levels in year

185 2013, and weaker anthropogenic emission levels in year 2017) can be analyzed as the

186 differences between BASE_17E17M and NOALL_17E17M (BASE_17E17M minus

187 NOALL_17E17M, denote as $\Delta O_3\_ARI_{17E}$), and BASE_13E17M and

188 NOALL_13E17M (BASE_13E17M minus NOALL_13E17M, denote as $\Delta O_3\_ARI_{13E}$).

189 Thus, the impact of weakened ARI due to clean air action on O_3 (denote as
190 $\Delta O_3\_\Delta ARI\_EMI$) can be quantified from the differences between $\Delta O_3\_ARI_{17E}$ and
191 $\Delta O_3\_ARI_{13E}$. Similarly, the impacts of weakened API (denote as $\Delta O_3\_\Delta API\_EMI$) and
192 ARF (denote as $\Delta O_3\_\Delta ARF\_EMI$) due to decreased anthropogenic emission on O_3 can
193 also be estimated from the differences between (BASE_17E17M minus
194 NOAPI_17E17M, denote as $\Delta O_3\_API_{17E}$) and (BASE_13E17M minus
195 NOAPI_13E17M, denote as $\Delta O_3\_API_{13E}$), and between (NOAPI_17E17M minus
196 NOALL_17E17M, denote as $\Delta O_3\_ARF_{17E}$) and (NOAPI_13E17M minus
197 NOALL_13E17M, denote as $\Delta O_3\_ARF_{13E}$), respectively. Detailed descriptions can be
198 found in Fig. 1.

199 Simulation periods are integrated from 30 May to 30 June (denoted as summer)
200 and 29 November to 31 December (denoted as winter) both in 2013 and 2017. To avoid
201 potential deviations caused by long-term model integration, each simulation is re-
202 initialized every eight days, with the first 40 hours as the model spin-up. The complete
203 simulation includes five model cycles. Simulation results from the BASE_17E17M
204 case during summer and winter are used to evaluate the model performance. If not
205 otherwise specified, the time in this paper is the local time, and the synergetic impacts
206 of ARF and API are equal to the impact of ARI (i.e., ARI=ARF+API).

207 2.3 Observational data

208 Meteorological observations of temperature (T_2), relative humidity (RH_2), wind
209 speed (WS_{10}) and wind direction (WD_{10}) provided by the NOAA's National Climatic
210 Data Center (https://www.ncei.noaa.gov/) are used to validate the model
211 meteorological performance. In this study, 353 stations are selected and the locations
212 are shown as red dots in Fig. S1. Observed surface $PM_{2.5}$, O_3 and NO_2 concentrations
213 in eastern China are obtained from the China National Environmental Monitoring
214 Center, which can be downloaded from http://beijingair.sinaapp.com. To ensure the
215 data quality, a single site with at least 500 actual observations during the simulated
216 period are used for model evaluation. A total of 1296 sites, as shown in Fig. 2a, are
217 obtained. Photolysis rates of nitrogen dioxide (NO_2) ($J[NO_2]$) measured at the Peking

218 University site (39.99 °N, 116.31 °E) are also used to evaluate the model performance.

219 2.4 Integrated process rate analysis

220 In order to quantitatively elucidate individual contributions of physical and

221 chemical processes to O_3 concentration changes due to weakened ARI, the integrated

222 process rate (IPR) methodology is applied in this study. IPR analysis is an advanced

223 tool to evaluate the key process for O_3 concentration variation (Shu et al., 2016; Zhu et

224 al., 2021; Yang et al., 2022). In this study, the IPR analysis tracks hourly (e.g., one time

225 step) contribution to O_3 concentration variation from four main processes, including

226 vertical mixing (VMIX), net chemical production (CHEM), horizontal advection

227 (ADVH), and vertical advection (ADVZ). We define ADV as the sum of ADVH and

228 ADVZ.

229 **3. Model Evaluation**

230 Simulation results of BASE_17E17M are used to compare with the observations

231 to evaluate the model performs before interpreting the impacts of aerosol-radiation

232 interaction on surface-layer ozone concentration.

233 3.1 Evaluation for meteorology

234 Figure S2 shows the time series of observed and simulated T_2, RH_2, WS_{10}, and

235 WD_{10} averaged over the 353 meteorological stations in China during summer and

236 winter in 2017. Statistical performances of simulated meteorological parameters

237 compared with ground-based observations are shown in Table 2. Simulations track well

238 with observed T_2 with the correlation coefficient (R) of 0.99 and 0.92, but underestimate

239 T_2 with the mean bias (MB) of -1.0 and -2.0 K in summer and winter, respectively.

240 Simulated RH_2 agree reasonably well with observations with R of 0.97 and 0.87, and

241 small normalized mean biases (NMB) are found in summer and winter with values of

242 3.2% and 3.5%, respectively. WS_{10} is slightly overpredicted with the MB of 1.6-2.1 m

243 s^{-1}. The R and root-mean-square error (RMSE) of WS_{10} are 0.77-0.82 and 1.6-2.1 m s^{-}

244 ^{1}, respectively. Large bias in wind speed can be partly caused by unresolved

245 topographical features (Jimenez and Dudhia, 2012). The NMB of WD_{10} ranges from -

9

246   3.9% to -2.6% and the R ranges from 0.40 to 0.69, respectively. As shown in Fig. S3,

247   the predicted J[NO_2] match well with the observations with R of 0.93-0.94 and NMB

248   of 4.8%-12.3%. In general, the simulated meteorological variables fairly well

249   agreement with the observations.

250   3.2 Evaluation for air pollutants

251   Figure 2 shows the spatial-temporal variations of observed and simulated near-

252   surface $PM_{2.5}$, O_3 and NO_2 concentrations averaged over eastern China during summer

253   and winter in 2017. As demonstrated in Figs. 2(a1) and (c1), WRF-Chem model

254   reasonably well reproduces the spatial distribution of observed $PM_{2.5}$, with high values

255   over large city cluster. The predicted O_3 concentrations can also reproduce the spatial

256   variation of the observed concentrations (Figs. 2(a2) and (c2)). NO_2 is an important

257   precursor of O_3 and aerosol, a good performance on NO_2 is necessary. From Figs. 2(a3)

258   and (c3), the model can well reproduce the spatial distribution of observed NO_2.

259   Although the distributions of simulated air pollutants are in good with the observations,

260   biases still exist, which may be due to the uncertain in the emission inventories. Figures

261   2(b1-b3) and 2(d1-d3) show the temporal profiles of observed and simulated surface-

262   layer air pollutants averaged over monitoring sites and the grid cell containing the

263   monitor site in eastern China. The statistical metrics are also shown in Table 2. As

264   shown in Figs. 2(b1) and (d1), the model tracks well with the diurnal variation of $PM_{2.5}$

265   over the eastern China, with R of 0.63 and 0.80, respectively. But the model slightly

266   underestimates the concentrations of $PM_{2.5}$ with MB of -6.3 and -10.1 μg m^{-3},

267   respectively, in summer and winter. Simulated O_3 agree reasonably well with

268   observations with R of 0.90 and 0.86, and small MB are found in summer and winter

269   with values of -0.6 and 2.8 ppb, respectively. The model tracks the daily variation of

270   observed NO_2 reasonably well, with R of 0.73 and 0.83. But the model slightly

271   underestimates the NO_2 against measurements, with MB of -1.5 and -4.5 ppb,

272   respectively, in summer and winter. In general, WRF-Chem model can well reproduce

273   the features of observed meteorology and air pollutants over eastern China.

4. Results and Discussion

4.1 Impacts of changed meteorology and anthropogenic emission on O_3

The strategy of clean air action decreased the anthropogenic emission of NO_x, but the changes in anthropogenic VOCs emissions were unobvious (Fig. S4), which might influence the O_3 formation sensitive regime and the O_3 concentration. Figure 3 shows the spatial distributions of changed summer and winter MDA8 O_3 concentrations from 2013 to 2017 over eastern China, and the contributions of changed anthropogenic emissions alone and changed meteorological conditions alone. As shown in Fig. 3(b), the concentration of summer MDA8 O_3 from 2013 to 2017 was increased in city clusters, but it was decreased in rural regions. This discrepancy might be explained by the ozone formation regimes in urban (typically VOCs-limited) and rural (typically NO_x-limited) areas during summer (Li et al., 2019; Wang et al., 2019). Contrary to the phenomenon in summer, decreased anthropogenic emissions lead to a uniform increase in winter MDA8 O_3 over the whole eastern China (Fig. 3(e)). The different spatial variation characteristics in summer and winter could be explained by the different ozone formation regimes in winter (VOCs-limited) and summer (NO_x-limited) (Jin and Holloway, 2015). From Figs. 3(c) and (f), the impacts of changed meteorological conditions on MDA8 O_3 varied by regions, ranging from -24.9 (-14.0) to 17.0 (7.3) ppb in summer (winter).

The reductions in anthropogenic emissions from 2013 to 2017 will also lead to a decrease in $PM_{2.5}$ concentrations (Fig. S5), which can further affect the O_3 concentrations by weakened aerosol-radiation interaction (ARI). Further, we average the observed MDA8 O_3 concentrations of monitoring sites in the urban areas and the simulation value for the grid cell containing the monitoring site to examine the impacts of changed meteorological conditions, anthropogenic emissions and ARI on O_3 levels in densely populated urban areas (Fig. 4). Given that most of the monitoring stations with 5 years of continuous observations are located in urban areas. Therefore, these monitoring stations and the grid cells containing the monitoring stations can be considered as urban areas in this study (Liu and Wang, 2020b). As shown in Figs. 4(a1)

303 and (b1), the changes in observed MDA8 O_3 over urban areas in eastern China from

304 2013 to 2017 can be well captured by WRF-Chem both in summer and winter. In

305 summer, changed meteorological conditions from 2013 to 2017 has little impact on the

306 variations in MDA8 O_3 over the urban areas, while the contribution of emission

307 reductions to increased MDA8 O_3 is significant. In winter, changed meteorological

308 conditions is unfavorable for the increase in MDA8 O_3 from 2013 to 2017, indicating

309 the worsened ozone pollution driven by the changed anthropogenic emission. What's

310 more, the $\Delta O_3\_\Delta ARI\_EMI$ has significant effect on the increased MDA8 O_3 in summer

311 from 2013 to 2017 with the value of +1.77 ppb (87.6%), but its impacts in winter are

312 smaller, only +0.42 ppb (11.8%), which is consistent with the results in Li et al. (2021).

313 Meanwhile, the contributions of $\Delta O_3\_\Delta API\_EMI$ and $\Delta O_3\_\Delta ARF\_EMI$ to the increase

314 in O_3 concentration averaged over urban areas in eastern China are almost the same in

315 summer (0.79 vs. 0.98) and winter (0.20 vs. 0.22). The model can also capture the

316 changes in observed summer/winter MDA8 O_3 from 2013 to 2017 over urban areas in

317 the four city clusters (Figs. 4(a2-b5)), except BTH in summer. The reason for the

318 underestimation over BTH may be that this study did not consider the effect of changes

319 in aerosol heterogeneous reactions. Li et al. (2019) found that the weakened uptake of

320 HO_2 on aerosol surfaces was the main reason for the O_3 increase over BTH. In general,

321 we find that the enhancement of O_3 concentrations both in summer and winter is mainly

322 caused by the factor of reduced anthropogenic emissions. Furthermore, the

323 contributions of $\Delta O_3\_\Delta API\_EMI$ and $\Delta O_3\_\Delta ARF\_EMI$ to the increases in O_3

324 concentrations from 2013 to 2017 over urban areas are almost the same during summer

325 and winter.

326 4.2 Impacts of weakened aerosol-radiation interaction on O_3

327 　　Figures S6a (S7a) and S6b (S7b) present the spatial distribution of the impacts of

328 ARF, API and ARI on surface MDA8 O_3 concentrations in summer (winter) under

329 different anthropogenic emission conditions in year 2017 and 2013, respectively. As

330 shown in Fig. S6, summer MDA8 O_3 are significantly reduced over eastern China, ARF,

331 API and ARI decrease the surface MDA8 O_3 concentrations by 0.23 (0.59) ppb, 1.09

332 (1.54) ppb and 1.32 (2.13) ppb under low (high) anthropogenic emission conditions in

333 year 2017 (year 2013), respectively. The changes in MDA8 O_3 concentrations due to

334 aerosol-radiation interaction under low emission condition are weaker than that under

335 high emission condition. This is because the concentration of aerosols in year 2013 is

336 higher than that in year 2017, and then its impact on meteorological conditions and

337 $J[NO_2]$ is greater (Fig. S8). As shown in Fig. S7a, ARF, API and ARI decrease the

338 winter MDA8 O_3 concentrations by 0.38 ppb (-0.9%), 1.59 ppb (-4.1%) and 1.96 ppb

339 (-5.1%) in year 2017, respectively. Compared to the impacts under relatively high

340 anthropogenic emission conditions in year 2013, the reduction of surface MDA8 O_3

341 concentrations caused by ARF, API and ARI are also greater, with the values of 0.62

342 ppb (-1.6%), 1.98 ppb (-5.4%) and 2.59 ppb (-7.1%), respectively. Both API and ARF

343 reduce O_3 concentrations, and the reduction in O_3 caused by API is greater than that

344 caused by ARF both in summer and winter.

345   Further, the significant reduction in $PM_{2.5}$ due to clean air action (Fig. S5) will

346 lead to an increase in O_3 concentrations as the weakened effects of aerosols on O_3.

347 Therefore, this study further quantifies the effects of $\Delta O_3\_\Delta API\_EMI$,

348 $\Delta O_3\_\Delta ARF\_EMI$ and $\Delta O_3\_\Delta ARI\_EMI$ on O_3 air quality. As shown in Figs. 5(a1-a3),

349 the surface MDA8 O_3 in summer are increased over most of eastern China due to

350 $\Delta O_3\_\Delta API\_EMI$, $\Delta O_3\_\Delta ARF\_EMI$ and $\Delta O_3\_\Delta ARI\_EMI$. The largest increases in

351 MDA8 O_3 concentrations due to $\Delta O_3\_\Delta API\_EMI$ and $\Delta O_3\_\Delta ARF\_EMI$ are found in

352 the developed four city clusters, with the increase larger than 4 ppb. Overall,

353 $\Delta O_3\_\Delta API\_EMI$, $\Delta O_3\_\Delta ARF\_EMI$ and $\Delta O_3\_\Delta ARI\_EMI$ lead to the increase in

354 surface MDA8 O_3 by 0.36 ppb, 0.45 ppb and 0.81 ppb averaged over eastern China

355 during summer, respectively. As shown in Fig. 5(a4-a6), the $\Delta O_3\_\Delta API\_EMI$,

356 $\Delta O_3\_\Delta ARF\_EMI$ and $\Delta O_3\_\Delta ARI\_EMI$ can also cause an increase in winter MDA8 O_3

357 concentrations by 0.24 ppb, 0.39 ppb and 0.63 ppb, respectively. In general, weakened

358 aerosol-radiation interaction due to reduced anthropogenic emission from 2013 to 2017

359 can exacerbate ozone pollution both in summer and winter.

360   In order to explore the mechanism of the impacts of $\Delta O_3\_\Delta ARI\_EMI$ on MDA8

361   O_3, we resolve the changed O_3 into the contributions from chemical and physical

362   processes. Figure 6 presents the accumulated changes in O_3 and each process

363   contribution from 09:00 to 16:00 LST by the $\Delta O_3\_\Delta API\_EMI$, $\Delta O_3\_\Delta ARF\_EMI$ and

364    $\Delta O_3\_\Delta ARI\_EMI$ ($\Delta O_3\_\Delta ARI\_EMI=\Delta O_3\_\Delta API\_EMI+\Delta O_3\_\Delta ARF\_EMI$)   during

365   summer and winter. As shown in Fig 6, the enhanced chemical production is the

366   dominant process leading to the increase in O_3 concentrations over eastern China and

367   the four city clusters both in summer and winter. The leading factor of enhancement in

368   O_3 over BTH are inconsistent with that over eastern China, and the enhancement of O_3

369   concentration in BTH is mainly due to $\Delta O_3\_\Delta ARF\_EMI$. But the leading factor of

370   enhancement in O_3 over SCB are consistent with that in eastern China, the enhancement

371   of O_3 concentration is mainly due to $\Delta O_3\_\Delta API\_EMI$ both in summer and winter.

372   Moreover, the enhancement of O_3 concentration in BTH, YRD and PRD is mainly due

373   to $\Delta O_3\_\Delta ARF\_EMI$ during winter, which is opposite to that of eastern China. The

374   leading factors for the increase of O_3 concentration in different city clusters are different.

375   The enhancement of O_3 concentration in most areas is caused by $\Delta O_3\_\Delta API\_EMI$,

376   whereas the increase in O_3 concentration in BTH, YRD and PRD areas is dominated by

377    $\Delta O_3\_\Delta ARF\_EMI$ in winter. In general, the weakened aerosol-radiation interaction

378   caused by emission reduction would promote the chemical production of O_3 and

379   increase the O_3 concentrations over eastern China in summer and winter.

380   In order to explore the reason for the increase in O_3 chemical production, we

381   further analyzed the variation of HO_x ($HO+HO_2$) concentration from 2013 to 2017. As

382   the aerosol concentration decreases, its influence on solar radiation is weakened and

383   photolysis is enhanced, leading to an increase in HO_x levels. It can be seen from Fig.

384   S9 that the concentration of HO_x increases both in winter and summer. The increase in

385   HO_x will promote the conversion of NO to NO_2, which will lead to the accumulation

386   of O_3 concentration.

387   4.3 Impacts of weakened aerosol-radiation interaction on effectiveness of emission

388   reduction for O_3 air quality

389   Figure 7 shows the changed summer and winter surface-layer MDA8 O_3

390 concentrations caused by anthropogenic emission reduction from 2013 to 2017 with

391 (ΔO_3_EMI) and without (ΔO_3_NOARI) ARI, including the effects of weakened ARI on

392 the effectiveness of emission reduction for O_3 air quality (ΔO_3_ΔARI_EMI, which is

393 also equal to ΔO_3_EMI minus ΔO_3_NOARI). Comparing with Fig. 7(a1) and (a2) in

394 summer and Fig. 7(a4) and (a5) in winter, when the impact of ARI is considered, the

395 concentrations of MDA8 O_3 are increased more than that when ARI is not taken into

396 account. Thus, ΔO_3_ΔARI_EMI makes the superimposed impact on the effectiveness

397 of anthropogenic emission reduction for the increased MDA8 O_3 concentrations from

398 2013 to 2017 over eastern China. However, during summer, the worsened O_3 air quality

399 due to weakened ARI can only be found in scattered city clusters (e.g., BTH, YRD and

400 PRD in Fig. 7(a3)). During winter, it would increase MDA8 O_3 concentrations over

401 nearly the whole eastern China (Fig. 7(a6)).

5 Conclusions

403 In this study, the impact of weakened aerosol-radiation interaction (ARI) due to

404 decreased anthropogenic emissions on surface O_3 (ΔO_3_ΔARI_EMI) over eastern

405 China is mainly analyzed by using an online-coupled regional chemistry transport

406 model WRF-Chem. Simulation results generally reproduce the spatiotemporal

407 characteristics of observations with correlation coefficients of 0.63-0.90 for pollutant

408 concentrations and 0.40-0.99 for meteorological parameters, respectively.

409 Sensitivity experiments show that the changes in MDA8 O_3 from 2013 to 2017

410 over eastern China vary spatially and seasonally, and the decreased anthropogenic

411 emission plays a more prominent role for the MDA8 O_3 increase than the impact of

412 changed meteorological conditions both in summer and winter. Furthermore, the

413 decreased $PM_{2.5}$ concentrations due to reduced anthropogenic emissions can result in a

414 weaker impact of ARI on O_3 concentrations, which finally pose a superimposed effect

415 on the worsened O_3 air quality. For urban areas over eastern China, ΔO_3_ΔARI_EMI

416 has a significant effect on the increase of MDA8 O_3 in summer with the value of +1.77

417 ppb, accounting for 87.6% of the increased value caused by decreased anthropogenic

418 emissions, but the impacts in winter are smaller (+0.42 ppb), accounting for 11.8% of

419 the increased value caused by decreased anthropogenic emissions. For the whole

420 regions over eastern China, the enhancement of MDA8 O_3 by $\Delta O_3\_\Delta ARI\_EMI$ is +0.81

421 (+0.63) ppb, with $\Delta O_3\_\Delta API\_EMI$ and $\Delta O_3\_\Delta ARF\_EMI$ contributing for 55.6%

422 (61.9%) and 44.4% (38.1%) in summer (winter), respectively. Process analysis shows

423 that the enhanced O_3 chemical production is the dominant process for the increased O_3

424 concentrations caused by $\Delta O_3\_\Delta ARI\_EMI$ both in summer and winter.

425 Generally, since China's clean air action from 2013, the decreased $PM_{2.5}$

426 concentrations due to reduced anthropogenic emissions can worsen O_3 air quality by

427 the weakened interactions between aerosol and radiation, which is a new and an

428 important implication for understanding the causes driving the increases in O_3 level

429 over eastern China. Therefore, our results highlight that more carefully designed multi-

430 pollutants coordinated emissions control strategies are needed to reduce the

431 concentrations of $PM_{2.5}$ and O_3 simultaneously.

432

Reference

Atkinson, R.: Atmospheric chemistry of VOCs and NOx, Atmos Environ., 34, 2063–2101, https://doi.org/10.1016/S1352-2310(99)00460-4, 2000.

Barnard, J. C., Fast, J. D., Paredes-Miranda, G., Arnott, W. P., and Laskin, A.: Technical Note: Evaluation of the WRF-Chem "Aerosol Chemical to Aerosol Optical Properties" Module using data from the MILAGRO campaign, Atmos. Chem. Phys., 10, 7325–7340, https://doi.org/10.5194/acp-10-7325-2010, 2010.

Chen, F. and Dudhia, J.: Coupling an Advanced Land Surface – Hydrology Model with the Penn State – NCAR MM5 Modeling System. Part I: Model Implementation and Sensitivity, Mon. Weather Rev., 129(4), 569–585, 2001.

Cheng, Y., Zheng, G., Chao, W., Mu, Q., Bo, Z., Wang, Z., Meng, G., Qiang, Z., He, K., and Carmichael, G.: Reactive nitrogen chemistry in aerosol water as a source of

Dang, R. and Liao, H.: Radiative Forcing and Health Impact of Aerosols and Ozone in China as the Consequence of Clean Air Actions over 2012–2017, Geophys. Res. Lett., 46, 12511–12519, https://doi.org/10.1029/2019GL084605, 2019.

Dickerson, R. R., Kondragunta, S., Stenchikov, G., Civerolo, K. L., Doddridge, B. G., and Holben, B. N.: The impact of aerosols on solar ultraviolet radiation and photochemical smog, Science, 278, 827-830, 10.1126/science.278.5339.827, 1997.

Foken, T.: 50 years of the Monin-Obukhov similarity theory, Bound.-Layer Meteor., 119, 431–437, 2006.

Grell G A.: Prognostic evaluation of assumptions used by cumulus parameterizations, Monthly Weather Review., 121, 764–787, 1993.

Grell, G. A., Peckham, S. E., Schmitz, R., Mckeen, S. A., Frost, G., Skamarock, K., and Eder, B.: Fully coupled "online" chemistry within the WRF model, Atmos. Environ., 39, 6957–6975, 2005.

Guenther, A., Karl, T., Harley, P., Wiedinmyer, C., Palmer, P. I., and Geron, C.: Estimates of global terrestrial isoprene emissions using MEGAN (Model of Emissions of Gases and Aerosols from Nature), Atmos. Chem. Phys., 6, 3181–3210, doi:10.5194/acp-6-3181-2006, 2006.

471   Hong, C., Zhang, Q., Zhang, Y., Davis, S. J., Zhang, X., Tong, D., Guan, D., Liu, Z.,
472   and He, K.: Weakening aerosol direct radiative effects mitigate climate penalty on
473   Chinese   air   quality,   Nat.   Clim.   Change,   10,   845–850,
474   https://doi.org/10.1038/s41558-020-0840-y, 2020.

475   Hong, S.-Y., Noh, Y., and Dudhia, J.: A New Vertical Diffusion Package with an
476   Explicit Treatment of Entrainment Processes, Mon. Weather Rev., 134, 2318–2341,
477   2006.

478   Iacono, M. J., Delamere, J. S., Mlawer, E. J., Shephard, M. W., Clough, S. A., and
479   Collins, W. D.: Radiative forcing by long-lived greenhouse gases: Calculations with
480   the   AER   radiative   transfer   models,   J.   Geophys.   Res.,   113,   D13103,
481   doi:10.1029/2008JD009944, 2008.

482   Jacob, D. J.: Heterogeneous chemistry and tropospheric ozone, Atmos. Environ., 34,
483   2131–2159, doi:10.1016/S1352- 2310(99)00462-8, 2000.

484   Jimenez, P. A. and Dudhia, J.: Improving the representation of resolved and unresolved
485   topographic effects on surface wind in the WRF model, J. Appl. Meteorol. Clim., 51,
486   300–316, 2012.

487   Jin, X. and Holloway, T.: Spatial and temporal variability of ozone sensitivity over
488   China observed from the Ozone Monitoring Instrument, J. Geophys. Res.-Atmos.,
489   120, 7229–7246, https://doi.org/10.1002/2015JD023250, 2015.

490   Lelieveld, J., Evans, J. S., Fnais, M., Giannadaki, D., and Pozzer, A.: The contribution
491   of outdoor air pollution sources to premature mortality on a global scale, Nature, 525,
492   367–371, https://doi.org/10.1038/nature15371, 2015.

493   Li, K., Jacob, D. J., Liao, H., Qiu, Y. L., Shen, L., Zhai, S. X., Bates, K. H., Sulprizio,
494   M. P., Song, S. J., Lu, X., Zhang, Q., Zheng, B., Zhang, Y. L., Zhang, J. Q., Lee, H.
495   C., and Kuk, K. S.: Ozone pollution in the North China Plain spreading into the late-
496   winter   haze   season,   118,   P.   Natl.   Acad.   Sci.   USA,
497   https://doi.org/10.1073/pnas.2015797118, 2021.

498   Li, K., Jacob, D. J., Liao, H., Shen, L., Zhang, Q., and Bates, K. H.: Anthropogenic
499   Drivers of 2013–2017 Trends in Summer Surface Ozone in China, P. Natl. Acad. Sci.

500   USA, 116, 422–427, https://doi.org/10.1073/pnas.1812168116, 2019.

501   Li, K., Jacob, D. J., Shen, L., Lu, X., De Smedt, I., and Liao, H.: Increases in surface

502   ozone pollution in China from 2013 to 2019: anthropogenic and meteorological

503   influences, Atmos. Chem. Phys., 20, 11423–11433, https://doi.org/10.5194/acp-20-

504   11423-2020, 2020.

505   Liao, H., Yung, Y. L., and Seinfeld, J. H.: Effects of aerosols on tropospheric photolysis

506   rates in clear and cloudy atmospheres, J. Geophys. Res., 104, 23697–23707, 1999.

507   Lin, Y.-L., Farley, R. D., and Orville, H. D.: Bulk parameterization of the snow field in

508   a cloud model, J. Clim. Appl. Meteorol., 22, 1065–1092, 1983.

509   Liu, Y. and Wang, T.: Worsening urban ozone pollution in China from 2013 to 2017 –

510   Part 1: The complex and varying roles of meteorology, Atmos. Chem. Phys., 20,

511   6305–6321, https://doi.org/10.5194/acp-20-6305-2020, 2020a.

512   Liu, Y. and Wang, T.: Worsening urban ozone pollution in China from 2013 to 2017 –

513   Part 2: The effects of emission changes and implications for multi-pollutant control,

514   Atmos. Chem. Phys., 20, 6323–6337, https://doi.org/10.5194/acp-20-6323-2020,

515   2020b.

516   Lou, S., Liao, H., and Zhu, B.: Impacts of aerosols on surface-layer ozone

517   concentrations in China through heterogeneous reactions and changes in photolysis

518   rates, Atmos. Environ., 85, 123–138, 2014.

519   Lu, X., Hong, J. Y., Zhang, L., Cooper, O. R., Schultz, M. G., Xu, X. B., Wang, T.,

520   Gao, M., Zhao, Y. H., and Zhang, Y. H.: Severe surface ozone pollution in China: A

521   global perspective, Environ. Sci. Tech. Lett., 5, 487–494,

522   https://doi.org/10.1021/acs.estlett.8b00366, 2018.

523   Mills, G., Sharps, K., Simpson, D., Pleijel, H., Broberg, M., Uddling, J., Jaramillo, F.,

524   Davies, W. J., Dentener, F., Van den Berg, M., Agrawal, M., Agrawal, S. B.,

525   Ainsworth, E. A., Buker, P., Emberson, L., Feng, Z., Harmens, H., Hayes, F.,

526   Kobayashi, K., Paoletti, E., and Van Dingenen, R.: Ozone pollution will compromise

527   efforts to increase global wheat production, Glob. Change Biol., 24, 3560–3574,

528   https://doi.org/10.1111/gcb.14157, 2018.

529   Seinfeld, J. H. and Pandis, S. N.: Atmospheric Chemistry and Physics: from Air

530   Pollution to Climate Change, second ed., John Wiley and Sons, 2006.

531   Shao, M., Wang, W. J., Yuan, B., Parrish, D. D., Li, X., Lu, K. D., Wu, L. L., Wang,

532   X. M., Mo, Z. W., Yang, S. X., Peng, Y. W., Kuang, Y., Chen, W. H., Hu, M., Zeng,

533   L. M., Su, H., Cheng, Y. F., Zheng, J. Y., Zhang, Y. H.: Quantifying the role of $PM_{2.5}$

534   dropping in variations of ground-level ozone: Inter-comparison between Beijing and

535   Los Angeles, Sci. Total Environ., https://doi.org/10.1016/j.scitotenv.2021.147712,

536   2021.

537   Shu, L., Wang, T., Han, H., Xie, M., Chen, P., Li, M., and Wu, H.: Summertime ozone

538   pollution in the Yangtze River Delta of eastern China during 2013–2017: Synoptic

539   impacts   and   source   apportionment,   Environ.   Pollut.,   257,   113631,

540   https://doi.org/10.1016/j.envpol.2019.113631, 2020.

541   Shu, L., Xie, M., Wang, T., Gao, D., Chen, P., Han, Y., Li, S., Zhuang, B., and Li, M.:

542   Integrated studies of a regional ozone pollution synthetically affected by subtropical

543   high and typhoon system in the Yangtze River Delta region, China, Atmos. Chem.

544   Phys., 16, 15801–15819, https://doi.org/10.5194/acp-16-15801- 2016, 2016.

545   Skamarock, W., Klemp, J. B., Dudhia, J., Gill, D. O., Barker, D. M., Duda, M., Huang,

546   X. Y., Wang,W., and Powers, J. G.: A description of the advanced research WRF

547   version 3, NCAR technical note NCAR/TN/u2013475, 2008.

548   sulfate   during   haze   events   in   China,   Science   Advances,   2,

549   https://doi.org/10.1126/sciadv.1601530, 2016.

550   Wang, J., Allen, D. J., Pickering, K. E., Li, Z., and He, H.: Impact of aerosol direct

551   effect on East Asian air quality during the EAST-AIRE campaign, J. Geophys. Res.-

552   Atmos., 121, https://doi.org/10.13016/M27W0S, 2016.

553   Wang, K., Zhang, Y., Nenes, A., and Fountoukis, C.: Implementation of dust emission

554   and chemistry into the Community Multiscale Air Quality modeling system and

555   initial application to an Asian dust storm episode, Atmos. Chem. Phys., 12, 10209–

556   10237, doi:10.5194/acp-12-10209-2012, 2012.

557   Wang, N., Lyu, X., Deng, X., Huang, X., Jiang, F., and Ding, A.: Aggravating O3

558   pollution due to NOx emission control in eastern China, Sci. Total Environ., 677,

559   732–744, 2019.

Wild, O., Zhu, X., and Prather, M. J.: Fast-J: Accurate simulation of in- and below-cloud photolysis in tropospheric chemical models, J. Atmos. Chem., 37, 245–282, doi:10.1023/A:1006415919030, 2000.

Yang, H., Chen, L., Liao, H., Zhu, J., Wang, W., and Li, X.: Impacts of aerosol–photolysis interaction and aerosol–radiation feedback on surface-layer ozone in North China during multi-pollutant air pollution episodes, Atmos. Chem. Phys., 22, 4101–4116, https://doi.org/10.5194/acp-22-4101-2022, 2022.

Yue, X., Unger, N., Harper, K., Xia, X., Liao, H., Zhu, T., Xiao, J., Feng, Z., and Li, J.: Ozone and haze pollution weakens net primary productivity in China, Atmos. Chem. Phys., 17, 6073–6089, https://doi.org/10.5194/acp-17-6073-2017, 2017.

Zaveri, R. A. and Peters, L. K.: A new lumped structure photochemical mechanism for large-scale applications, J. Geophys. Res., 104, D23, 30387–30415, https://doi.org/10.1029/1999JD900876, 1999.

Zaveri, R. A., Easter, R. C., Fast, J. D., and Peters, L. K.: Model for simulating aerosol interactions and chemistry (MOSAIC), J. Geophys. Res., 113, D13204, https://doi.org/10.1029/2007JD008782, 2008.

Zhai, S., Jacob, D. J., Wang, X., Shen, L., Li, K., Zhang, Y., Gui, K., Zhao, T., and Liao, H.: Fine particulate matter (PM2.5) trends in China, 2013–2018: separating contributions from anthropogenic emissions and meteorology, Atmos. Chem. Phys., 19, 11031–11041, https://doi.org/10.5194/acp-19-11031-2019, 2019.

Zhang, Q., Zheng, Y., Tong, D., Shao, M., Wang, S., Zhang, Y., Xu, X., Wang, J., He, H., Liu, W., Ding, Y., Lei, Y., Li, J., Wang, Z., Zhang, X., Wang, Y., Cheng, J., Liu, Y., Shi, Q., Yan, L., Geng, G., Hong, C., Li, M., Liu, F., Zheng, B., Cao, J., Ding, A., Gao, J., Fu, Q., Huo, J., Liu, B., Liu, Z., Yang, F., He, K., and Hao, J.: Drivers of Improved PM2.5 Air Quality in China from 2013 to 2017, P. Natl. Acad. Sci. USA, 116, 24463–24469, https://doi.org/10.1073/pnas.1907956116, 2019.

Zhang, Y. and Carmichael, G. R.: The Role of Mineral Aerosol in Tropospheric Chemistry in East Asia—A Model Study, J. Appl. Meteorol., 38, 353–366, doi:10.1175/1520- 0450(1999)0382.0.co;2, 1999.

Zheng, B., Tong, D., Li, M., Liu, F., Hong, C., Geng, G., Li, H., Li, X., Peng, L., Qi, J.,

590   Yan, L., Zhang, Y., Zhao, H., Zheng, Y., He, K., and Zhang, Q.: Trends in China's

591   anthropogenic emissions since 2010 as the consequence of clean air actions, Atmos.

592   Chem. Phys., 18, 14095–14111, https://doi.org/10.5194/acp-18-14095-2018, 2018.

593   Zheng, B., Zhang, Q., Zhang, Y., He, K. B., Wang, K., Zheng, G. J., Duan, F. K., Ma,

594   Y. L., and Kimoto, T.: Heterogeneous chemistry: a mechanism missing in current

595   models to explain secondary inorganic aerosol formation during the January 2013

596   haze episode in North China, Atmos. Chem. Phys., 15, 2031–2049,

597   https://doi.org/10.5194/acp-15-2031-2015, 2015.

598   Zhu, J., Chen, L., Liao, H., Yang, H., Yang, Y., and Yue, X.: Enhanced PM2.5

599   Decreases and O3 Increases in China During COVID-19 Lockdown by Aerosol-

600   Radiation   Feedback,   Geophys.   Res.   Lett.,   48,

601   https://doi.org/10.1029/2020GL090260, 2021.

602

603   **Table 1.** Descriptions of model sensitivity experiments.

Cases	Anthropogenic emission	Meteorological field	API[a]	ARF[a]
BASE_17E17M	2017	2017	On	On
BASE_13E13M	2013	2013	On	On
NOAPI_17E17M	2017	2017	Off	On
NOALL_17E17M	2017	2017	Off	Off
BASE_13E17M	2013	2017	On	On
NOAPI_13E17M	2013	2017	Off	On
NOALL_13E17M	2013	2017	Off	Off

604   [a]API means aerosol-photolysis interaction, ARF means aerosol-radiation feedback.

605

Table 2. Statistical parameters of the simulated 2 m temperature (T_2, k), 2 m relative humidity (RH_2, %), 10 m wind speed (WS_{10}, m s⁻¹), 10 m wind direction (WD_{10}, °), photolysis rate of NO_2 ($J[NO_2]$, 10^{-3} s⁻¹), $PM_{2.5}$ (μg m⁻³), O_3 (ppb), and NO_2 (ppb) against observations during summer and winter in 2017.

Variable	Summer						Winter					
	O^a	M^a	R^b	MB^c	NMB^d (%)	$RMSE^e$	O^a	M^a	R^b	MB^c	NMB^d (%)	$RMSE^e$
T_2	295.3	294.2	0.99	-1.0	-3.2	1.0	275.0	272.8	0.92	-2.0	-74.1	2.5
RH_2	68.1	71.0	0.97	2.2	3.2	3.6	58.1	60.6	0.87	2.1	3.5	6.5
WS_{10}	2.6	4.2	0.77	1.6	61.6	1.6	2.6	4.7	0.82	2.1	83.2	2.1
WD_{10}	175.7	170.9	0.40	-4.6	-2.6	16.9	192.6	184.6	0.69	-7.5	-3.9	17.4
$J[NO_2]$	2.6	2.7	0.93	0.1	4.8	1.2	1.0	1.2	0.94	0.1	12.3	0.6
$PM_{2.5}$	31.0	24.8	0.63	-6.3	-20.2	8.3	69.0	58.9	0.80	-10.1	-14.6	15.6
O_3	39.7	38.9	0.90	-0.6	-1.6	6.9	17.7	20.5	0.86	2.8	15.7	5.0
NO_2	12.7	11.2	0.73	-1.5	-12.0	4.5	23.3	18.7	0.83	-4.5	-19.4	5.6

ᵃ O and M are the averages for observed and simulated results, respectively. $O = \frac{1}{n} \times \sum_{i=1}^{n} O_i$, $M = \frac{1}{n} \times \sum_{i=1}^{n} M_i$.

ᵇ R is the correlation coefficient between observations and model results. $R = \frac{\sum_{i=1}^{n} |(O_i - \overline{O}) \times (M_i - \overline{M})|}{\sqrt{\sum_{i=1}^{n} (O_i - \overline{O})^2 + \sum_{i=1}^{n} (M_i - \overline{M})^2}}$.

ᶜ MB is the mean bias between observations and model results. $MB = \frac{1}{n} \times \sum_{i=1}^{n} (M_i - O_i)$.

ᵈ NMB is the normalized mean bias between observations and model results. $NMB = \frac{1}{n} \times \sum_{i=1}^{n} \frac{M_i - O_i}{O_i} \times 100\%$.

ᵉ $RMSE$ is the root-mean-square error of observations and model results. $RMSE = \sqrt{\frac{1}{n} \times \sum_{i=1}^{n} (M_i - O_i)^2}$.

In the above O_i and M_i are the hourly observed and simulated data, respectively, and n is the total number of hours.
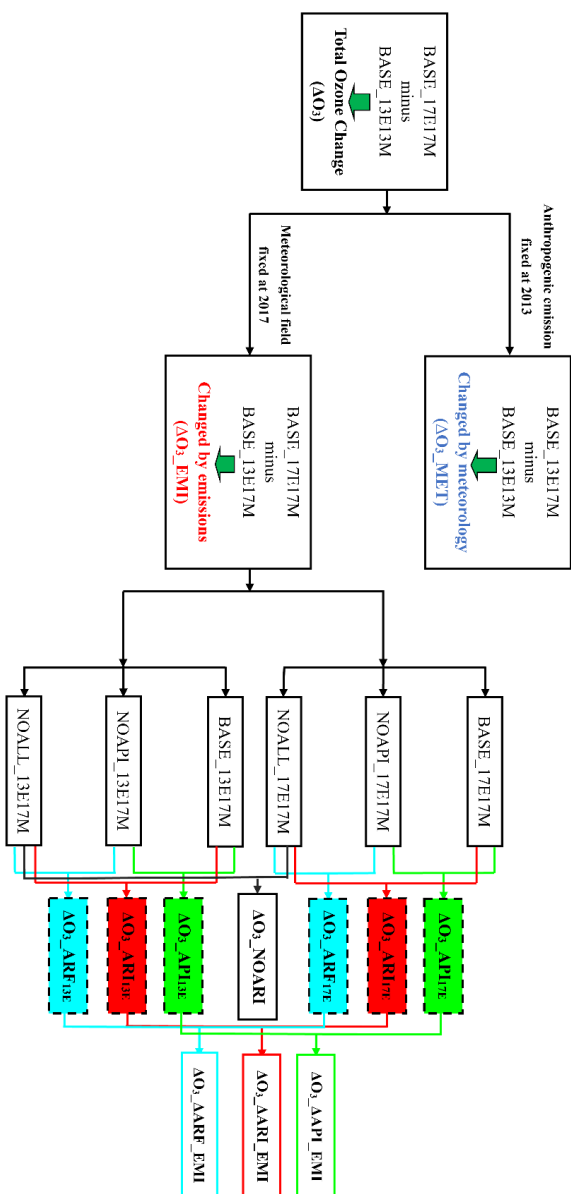
Figure 1. Schematic overview of numerical experiments. 17E17M (13E13M) means meteorological fields and anthropogenic emissions are fixed at year 2017 (2013). 13E17M means anthropogenic emissions are fixed at year 2013 but meteorological fields are at year 2017. ΔO_3_MET, ΔO_3_EMI and ΔO_3 mean the impacts of changed meteorological conditions, changed anthropogenic emissions and their combined effects on O_3, respectively. $\Delta O_3\_APL_{17E(13E)}$, $\Delta O_3\_ARF_{17E(13E)}$ and $\Delta O_3\_ARI_{17E(13E)}$ mean the impacts of aerosol-photolysis interaction, aerosol-radiation feedback and aerosol-radiation interaction on O_3 under different emission conditions, respectively. ΔO_3_NOARI means the changed O_3 concentration by reduced anthropogenic emissions without considering aerosol-radiation interaction. $\Delta O_3\_\Delta APL\_EMI$, $\Delta O_3\_\Delta ARF\_EMI$ and $\Delta O_3\_\Delta ARI\_EMI$ represent the impacts of weakened aerosol-photolysis interaction, aerosol-radiation feedback and aerosol-radiation interaction due to decreased anthropogenic emission on O_3 concentration, respectively.
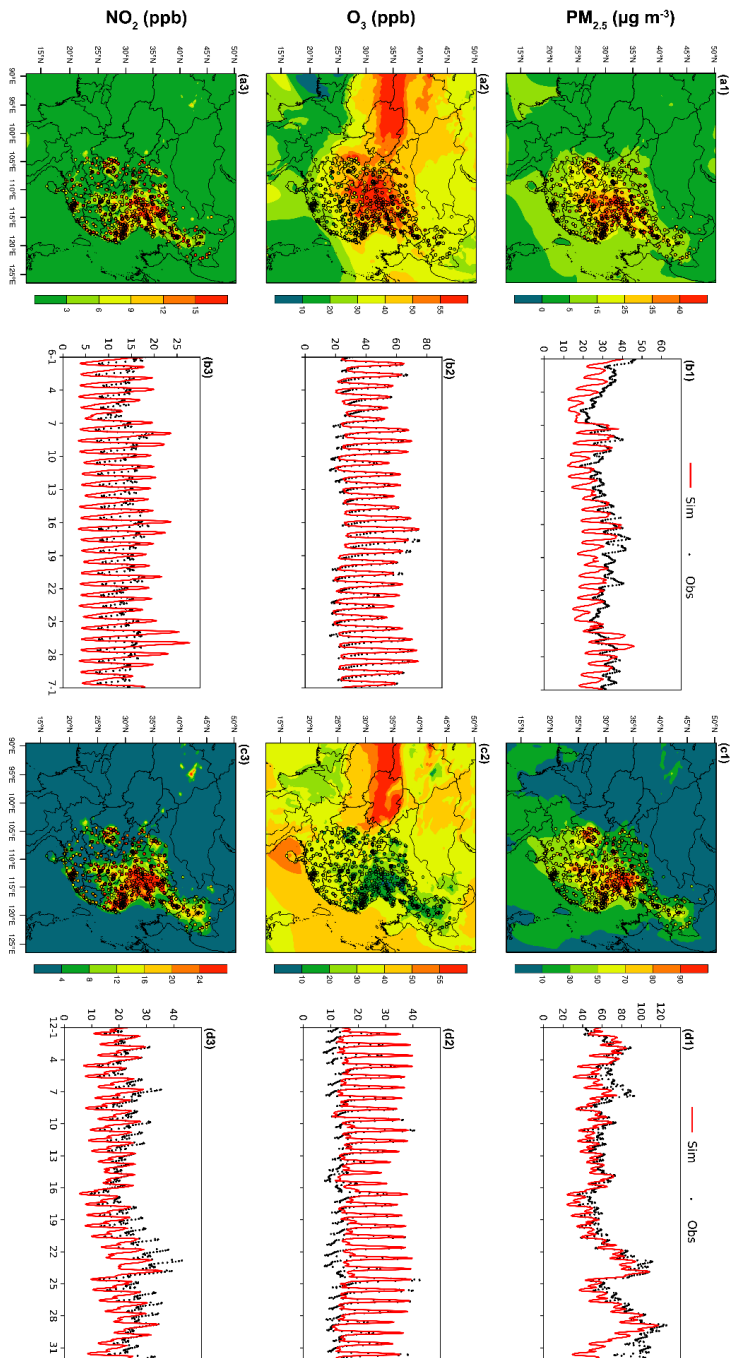
Figure 2. Spatial distributions of observed (circle) and simulated (shade) PM$_{2.5}$, O$_3$ and NO$_2$ concentrations averaged over (**a1–a3**) summer and (**c1–c3**) winter in 2017. Time series of observed (black dots) and simulated (red lines) hourly PM$_{2.5}$, O$_3$ and NO$_2$ concentrations averaged over the whole observation sites in eastern China during (**b1–b3**) summer and (**d1–d3**) winter in 2017.
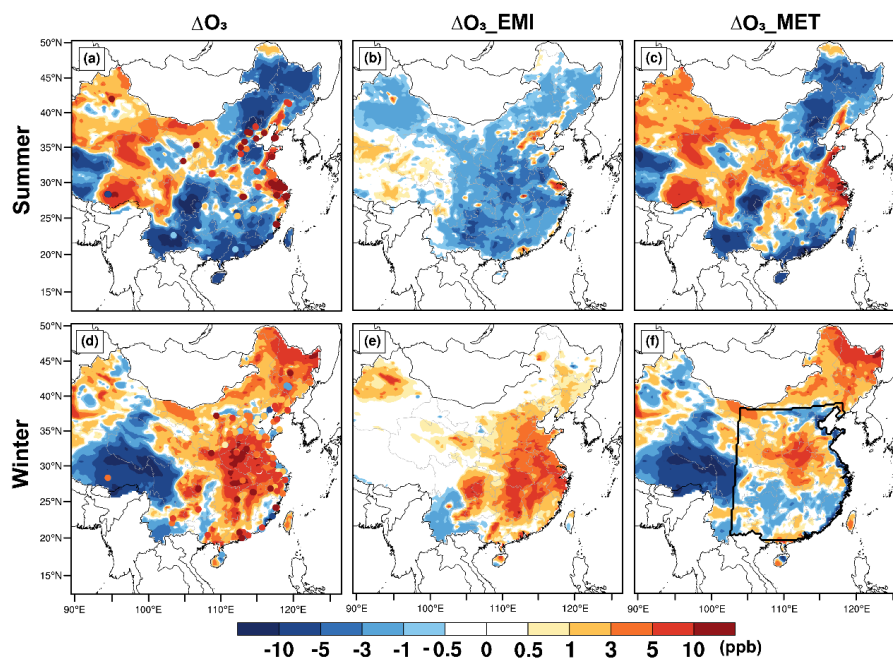
Figure 3. (a, d) Spatial distribution of changed summer (upper) and winter (bottom) surface-layer MDA8 O_3 from 2013 to 2017, and the contributions of **(b, e)** changed anthropogenic emissions alone and **(c, f)** changed meteorological fields alone. The observed changes in surface MDA8 O_3 are also marked with colored circles in **(a)** and **(d)**. The enclosed black line in **(f)** represents eastern China.
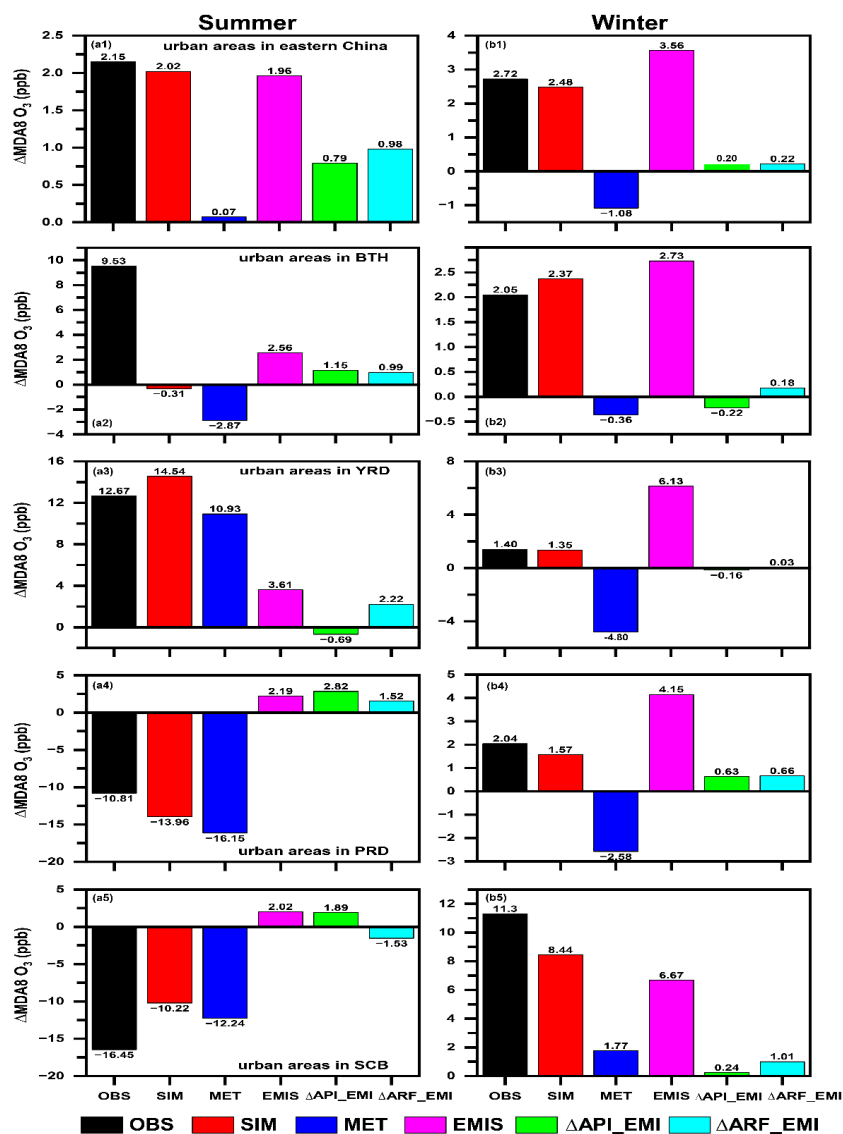
Figure 4. The observed (OBS, black bars) and simulated (SIM, red bars) changes in (left) summer and (right) winter surface-layer MDA8 O₃ from 2013 to 2017. Contributions of changed meteorological conditions alone (MET, blue bars), changed anthropogenic emissions alone (EMI, purple bars), changed aerosol-photolysis interaction alone (ΔAPI_EMI, green bars), and changed aerosol-radiation feedback alone (ΔARF_EMI, cyan bars) are also shown. Observations are calculated from the monitoring sites in the analyzed region, while the corresponding gridded simulations are averaged for SIM. **(a1-b1)**, **(a2-b2)**, **(a3-b3)**, **(a4-b4)** and **(a5-b5)** represent the urban areas in eastern China, Beijing-Tianjin-Hebei (BTH), Yangtze River Delta (YRD), Pearl River Delta (PRD), and Sichuan Basin (SCB), respectively.
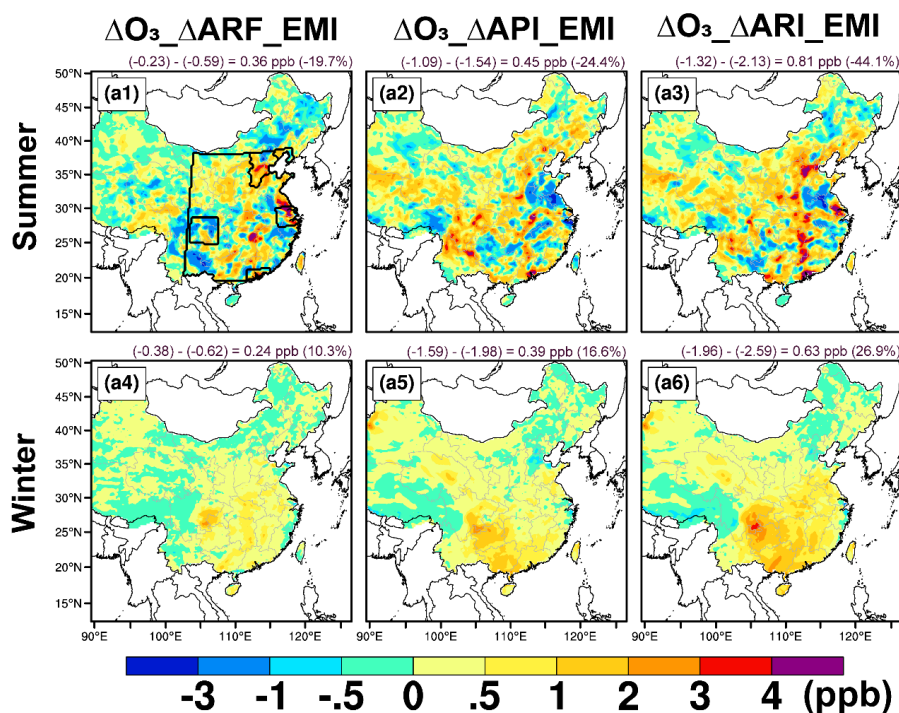
Figure 5. Impacts of $\Delta O_3\_\Delta ARF\_EMI$, $\Delta O_3\_\Delta API\_EMI$, and $\Delta O_3\_\Delta ARI\_EMI$ on summer (upper) and winter (bottom) surface-layer MDA8 O_3 concentrations. The enclosed black line in **(a1)** represents eastern China and the four developed city clusters. The mean changes over eastern China are also shown at the top of each panel. Detailed information about $\Delta O_3\_\Delta ARF\_EMI$, $\Delta O_3\_\Delta API\_EMI$, and $\Delta O_3\_\Delta ARI\_EMI$ can be found in Figure 1.
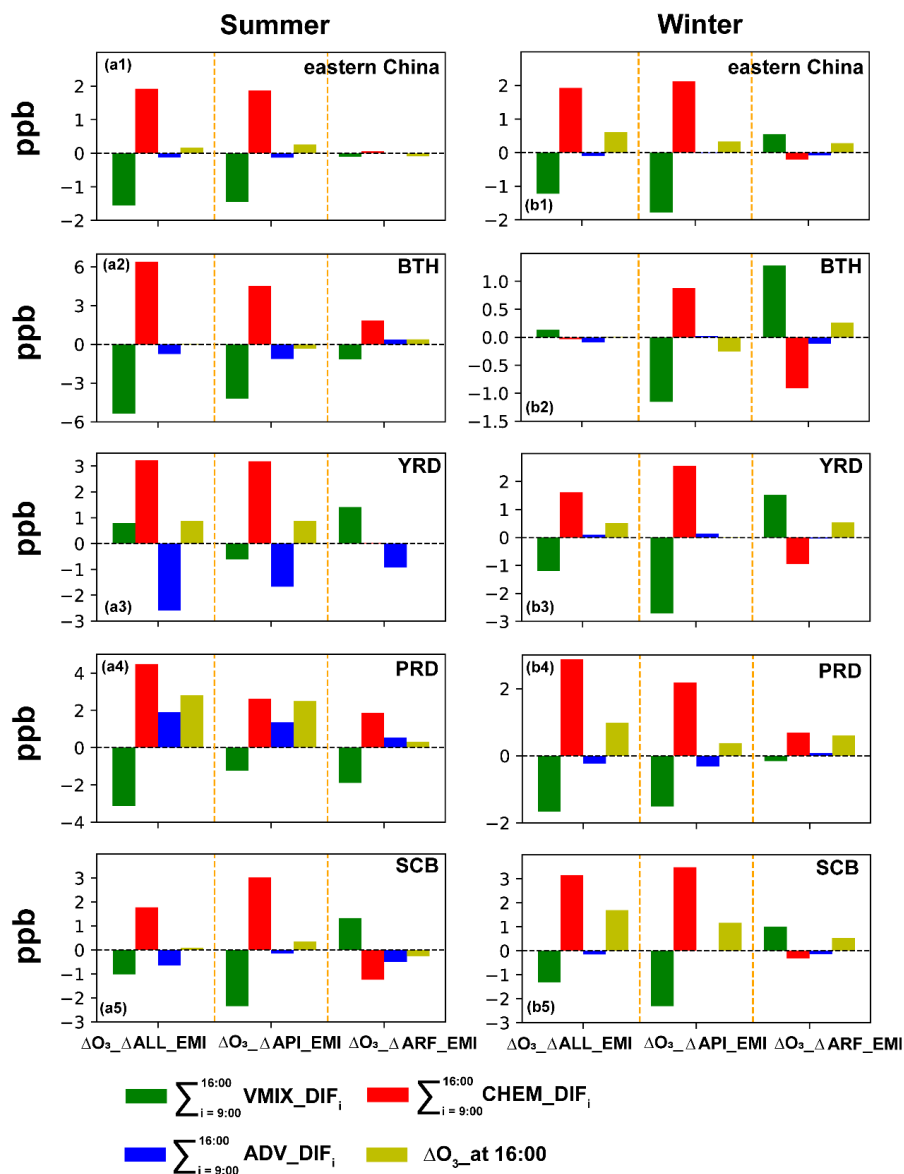
Figure 6. Accumulated changes in each process from 09:00 to 16:00 LST and the changed O_3 concentrations due to $\Delta O_3\_\Delta ARI\_EMI$ in summer (left column) and winter (right column). The regions of eastern China, Beijing-Tianjin-Hebei (BTH), Yangtze River Delta (YRD), Pearl River Delta (PRD) and Sichuan Basin (SCB) are indicated on the right side of each panel.
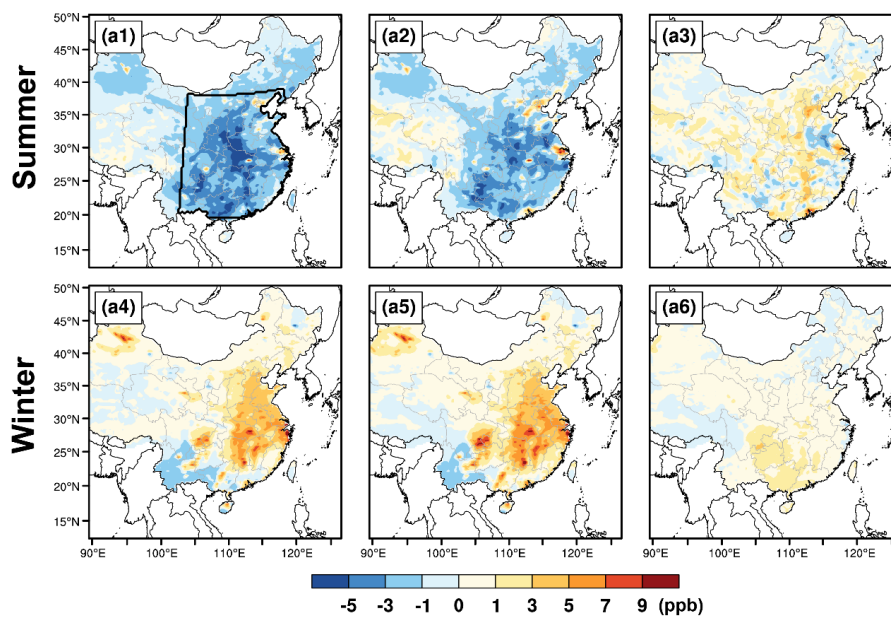
Figure 7. Spatial distribution of changed summer (upper) and winter (bottom) surface-layer MDA8 O_3 concentrations from sensitivity simulations. **(a1, a4)** Effects of anthropogenic emission reduction on MDA8 O_3 without ARI. **(a2, a5)** Effects of anthropogenic emission reduction on MDA8 O_3 with ARI. **(a3, a6)** Effects of weakened ARI on the effectiveness of emission reduction for O_3 air quality.